



Cite this: *Phys. Chem. Chem. Phys.*, 2024, 26, 18799

# The thermodynamics of self-assembled monolayer formation: a computational and experimental study of thiols on a flat gold surface†

Alberto Zoccante,<sup>a</sup> Eleonora Cara,<sup>b</sup> Federico Ferrarese Lupi,<sup>b</sup> Philipp Hönicke,<sup>ce</sup> Yves Kayser,<sup>cf</sup> Burkhard Beckhoff,<sup>c</sup> Petr Klapetek,<sup>d</sup> Davide Marchi<sup>a</sup> and Maurizio Cossi<sup>a</sup>

A methodology based on molecular dynamics simulations is presented to determine the chemical potential of thiol self-assembled monolayers on a gold surface. The thiol de-solvation and then the monolayer formation are described by thermodynamic integration with a gradual decoupling of one molecule from the environment, with the necessary corrections to account for standard state changes. The procedure is applied both to physisorbed undissociated thiol molecules and to chemisorbed dissociated thiyl radicals, considering in the latter case the possible chemical potential of the produced hydrogen. We considered monolayers formed by either 7-mercapto-4-methylcoumarin (MMC) or 3-mercapto-propanoic acid (MPA) on a flat gold surface: the free energy profiles with respect to the monolayer density are consistent with a transition from a very stable lying-down phase at low densities to a standing-up phase at higher densities, as expected. The maximum densities of thermodynamically stable monolayers are compared to experimental measures performed with reference-free grazing-incidence X-ray fluorescence (RF-GIXRF) on the same systems, finding a better agreement in the case of chemisorbed thiyl radicals.

Received 29th March 2024,  
Accepted 11th June 2024

DOI: 10.1039/d4cp01322k

[rsc.li/pccp](http://rsc.li/pccp)

## 1 Introduction

Self-assembled monolayers (SAMs) represent a good example of the spontaneous formation of complex nanometer-sized structures from simpler subunits. SAMs are typically constituted by molecules adsorbed on a solid surface, and many chemical headgroups are suitable for the preparation of such ordered layers. Thiols, dithiols and other sulfur compounds are particularly popular for nanotechnological applications owing to their ability to readily form SAMs over oxide-free metal surfaces.

Thiol self-assembled monolayers (SAMs) on gold and, to a lesser extent, silver surfaces have been intensively studied for their important applications in nanotechnology. Specific applications include their use as inks or resists in lithography,<sup>1–6</sup> as passive or active components in molecular electronics,<sup>7–12</sup> and in sensors or biosensors<sup>13–16</sup> (see ref. 17 for a comprehensive review).

While the kinetics of thiol SAM formation has been deeply studied over the years, some uncertainty remains about its actual mechanism.<sup>17–19</sup> Most investigations assume chemical interactions, *i.e.* the formation of a S–Au covalent bond (chemisorption), to be at the base of the stability of thiol SAMs. In particular, it is assumed that the thiol hydrogen atoms react upon adsorption to evolve as H<sub>2</sub>, hence facilitating the formation of a strong S–Au bond. However, other recent studies suggest that non-dissociative adsorption (physisorption), which preserves the S–H bond in SAMs, may also occur. For instance, programmed temperature desorption experiments failed to detect the formation of disulfides (as one would expect from desorption in the absence of remaining S–H bonds).<sup>20</sup> Single molecule conductance measurements also seem to detect physisorbed molecules rather than chemisorbed ones.<sup>19</sup> While different studies have attempted to clarify this issue, and at least in one case<sup>21</sup> some indication of the formation of free hydrogen has been provided, to our knowledge a deep

<sup>a</sup> Dipartimento di Scienze e Innovazione Tecnologica (DISIT), Università del Piemonte Orientale, via T. Michel 11, I-15121 Alessandria, Italy.

E-mail: [alberto.zoccante@uniupo.it](mailto:alberto.zoccante@uniupo.it)

<sup>b</sup> Istituto Nazionale di Ricerca Metrologica (INRiM), Strada delle Cacce, 91, 10135 Torino, Italy

<sup>c</sup> Physikalisch-Technische Bundesanstalt (PTB), Abbestr. 2-12, 10587 Berlin, Germany

<sup>d</sup> Department of Nanometrology, Czech Metrology Institute (CMI), Okružní 31, 638 00 Brno, Czech Republic

<sup>e</sup> Helmholtz-Zentrum Berlin, Hahn-Meitner Platz 1, 14109 Berlin, Germany

<sup>f</sup> Max-Planck-Institut für chemische Energiekonversion Mulheim an der Ruhr, Nordrhein-Westfalen, DE, Germany

† Electronic supplementary information (ESI) available. See DOI: <https://doi.org/10.1039/d4cp01322k>



understanding of the SAM formation mechanism and energetics is still lacking.

Thiol SAMs have been extensively studied from a computational perspective too:<sup>22–26</sup> most calculations dealt with possible chemisorption mechanisms and energetics, whereas the works on SAM thermodynamic stability are rarer.<sup>27,28</sup> In particular, a detailed comparison of the thermodynamics of physisorbed and chemisorbed SAMs has not been presented yet, though this information could provide very useful insights about the nature of the monolayers. In the present work, we propose such a detailed analysis by computing the chemical potentials of physisorbed and chemisorbed SAMs at different layer densities, considering non-crystalline SAMs, in a similar fashion as in a recent study about the relative stability of SAM polymorphs.<sup>27</sup>

Classical molecular dynamics (MD) has been long used for the computation of free energy differences in biophysics: for instance, binding free energies have been computed for ligand–enzyme complexes with MD simulations since the beginning of the 1980s,<sup>29–33</sup> as well as more recently for protein–protein or protein–nucleic acid complexes.<sup>34</sup> So-called “alchemical” techniques have also been applied to the computation to molecular crystal solubilities,<sup>35–37</sup> as well as to the calculation of the adsorption free energies of catalytic species on metal surfaces.<sup>38</sup>

We applied a similar approach to compute the chemical potentials of SAMs formed by two different thiols, namely, 7-mercapto-4-methylcoumarin (MMC) and 3-mercapto-propanoic acid (MPA), either by physisorption (*i.e.* keeping the thiol S–H bond) or by chemisorption (breaking the S–H bond) at various densities: the molecular structures are illustrated in Fig. 1. The goal is to determine at which layer density the various SAMs become thermodynamically unstable (that is, their chemical potential becomes positive) and to compare these maximum theoretical densities with the density measured experimentally. If physisorbed/chemisorbed simulated layers have different maximum densities, such a comparison will provide an indication about the SAM nature.

Early studies of the structure of alkanethiol SAMs on flat gold surfaces proposed a  $(\sqrt{3} \times \sqrt{3})R30^\circ$  structure relative to the underlying Au(111) substrate,<sup>39</sup> corresponding to 4.6 molecules per nm<sup>2</sup>. Other values, however, were found with various experimental techniques, reaching, for instance, for MPA  $6.3 \pm 0.6$ <sup>40</sup> and  $7.8 \pm 1.2$ <sup>41</sup> molecules per nm<sup>2</sup>. Such a variety of data calls for more elaborated theoretical models, not based on simple

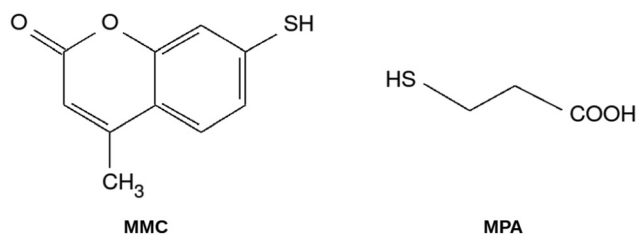


Fig. 1 Molecular structure of 7-mercapto-4-methylcoumarin (MMC) and 3-mercapto-propanoic acid (MPA). Radical thiyls are obtained by homolytic cleavage of the S–H bond.

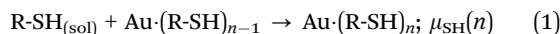
ordered lattices, but including thermal, steric and entropic effects as well, like the approach proposed in this work.

In the first part of the paper, we first review the thermodynamics of SAM formation and then proceed to describe a double-decoupling procedure to compute the chemical potentials of SAMs (Section 2). In Section 3, we describe the models and computational details, while in Section 4 we discuss the results of our investigation. Section 5 deals with conclusion and discusses directions for further work.

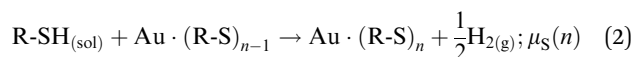
## 2 SAM formation thermodynamics

### 2.1 SAM formation thermodynamics

We consider two reactions in which one thiol molecule, originally in ethanol solution, enters into a pre-existing SAM:



and



Reaction (1) (Fig. 2(a)) describes the physisorption of one more thiol in a monolayer already containing  $(n - 1)$  thiol molecules; in reaction (2) (Fig. 2(b)) the S–H bond is broken generating a thiyl radical – which enters the chemisorbed SAM originally containing  $(n - 1)$  radicals – along with a hydrogen atom, eventually leading to gaseous H<sub>2</sub>. In both cases, the free energy difference between the reactants and products corresponds to the chemical potential ( $\mu_{\text{SH}}$  and  $\mu_{\text{S}}$ , respectively) at the surface density of  $n$  molecules or radicals per surface unit.

Note that, following the terminology adopted in ref. 42, we consider the dissociated species as a thiyl radical rather than a thiolate ion, unlike many other studies. In fact, the S–H bond

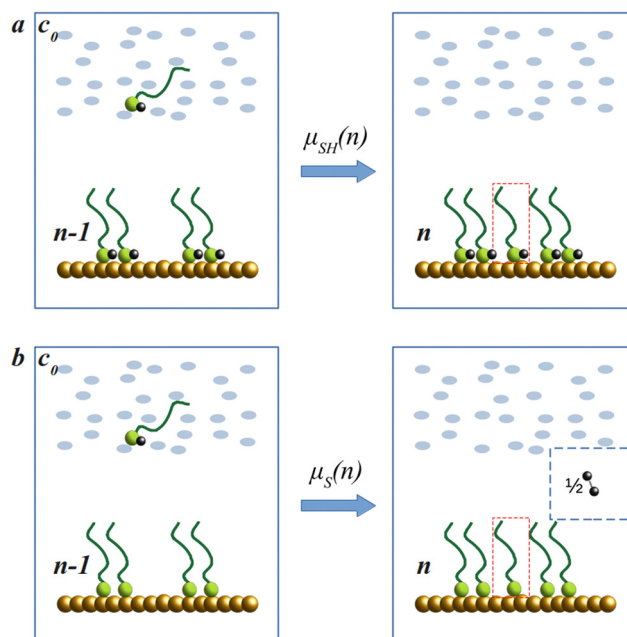


Fig. 2 Graphical representation of reaction (1) (a) and reaction (2) (b).



dissociates homolytically, and whether the R-S unit should be considered a radical or an ion depends on the charge distribution in the S-Au bond, which is of little importance for our purposes.

Classical statistical mechanics provides the starting point for the computation of (Helmholtz) free energy differences in terms of the configurational partition functions of reagents and products.

For the case of physisorbed SAMs, the chemical potential can be computed as

$$\mu_{\text{SH}}(n) = -RT \ln \frac{Z_n Z_{\text{sol}}}{Z_{\text{sol,SH},c_0} Z_{n-1}} \quad (3)$$

where  $Z_n$  and  $Z_{n-1}$  are the partition functions of SAMs with surface densities of  $n$  or  $n - 1$  molecules per (surface) cell, respectively,  $Z_{\text{sol}}$  is the partition function of the pure solvent, and  $Z_{\text{sol,SH},c_0}$  is the partition function of a solution of thiol with concentration  $c_0$ . Ideality is always assumed for gases and liquid solutions (meaning in the latter case that solute molecules do not interact with each other).

Following the double decoupling scheme, the logarithm in eqn (3) can be rewritten as

$$\ln \frac{Z_n Z_{\text{sol}}}{Z_{\text{sol,SH},c_0} Z_{n-1}} = \ln \frac{Z_n}{Z_{\text{g,SH},\rho_1} Z_{n-1}} + \ln \frac{Z_{\text{g,SH},\rho_1} Z_{\text{sol}}}{Z_{\text{sol,SH},c_0}} \quad (4)$$

That is

$$\mu_{\text{SH}}(n) = \Delta G_{\text{de-solv}}(c_0, \rho_1) + \Delta G_{\text{SAM}}^{(n)} \quad (5)$$

where  $\Delta G_{\text{de-solv}}$  is the free energy needed to extract the molecule from a solution with concentration  $c_0$  to an ideal gas phase of molar density  $\rho$  and  $\Delta G_{\text{SAM}}^{(n)}$  is the free energy needed to insert a molecule from the ideal gas at density  $\rho$  into a monolayer of surface density  $n$ .

These terms can be computed with MD techniques, as explained below, but some corrections are needed to take into account the changes in translational volumes: typically, the experimental concentration ( $c_0$ ) is not suited to a MD simulation (as it would require a very large simulation box), so a different, larger concentration ( $c_1$ ) is used to calculate the desolvation free energy. Hence, a correction term is added,

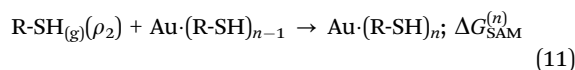
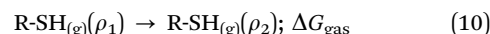
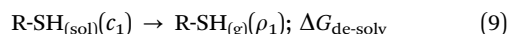
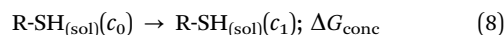
accounting for the reduction of the accessible translational volume:

$$\Delta G_{\text{conc}} = RT \ln(c_1/c_0) \quad (6)$$

Moreover, in our setup the simulation boxes for the desolvation and the insertion steps differ. Hence, a second volume term is needed to account for the difference between the density  $\rho_1$  of the ideal gas phase coming from the desolvation and the density  $\rho_2$  required for the insertion step:

$$\Delta G_{\text{gas}} = RT \ln(\rho_2/\rho_1) \quad (7)$$

Summarizing, reaction (1) is split into the following steps, whose  $\Delta G$  values are computed separately.



so that the final chemical potential is

$$\mu_{\text{SH}}(n) = \Delta G_{\text{conc}} + \Delta G_{\text{de-solv}} + \Delta G_{\text{gas}} + \Delta G_{\text{SAM}}^{(n)} \quad (12)$$

A visual representation of the setup is given in Fig. 3(a).

On the other hand, the chemical potential of chemisorbed SAMs can be written as

$$\mu_{\text{S}}(n) = -RT \ln \frac{Z_n Z_{\text{sol}} Z_{\text{H}_2, \text{gas}}}{Z_{\text{sol,SH},c_0} Z_{n-1}} \quad (13)$$

where  $Z_n$  and  $Z_{n-1}$  are the partition functions of thiol SAMs and  $Z_{\text{H}_2, \text{gas}}$  is the partition function of the molecular hydrogen produced in the chemisorption reaction.

The process can be split into successive steps following the same scheme as above, with an additional contribution accounting for the thiol dissociation in thiol and hydrogen,  $\Delta G_{\text{diss}}$ . Thiol dissociation produces molecular hydrogen at half the concentration of the thiol ( $\rho_1$ ); then,  $\text{H}_2$  is expected to evolve from the reaction site to a final density  $\rho_{\text{H}_2}$ , so that another concentration term is needed,  $\Delta G_{\text{gas, H}_2} = \frac{1}{2} RT \ln \frac{\rho_{\text{H}_2}}{\rho_1}$ .

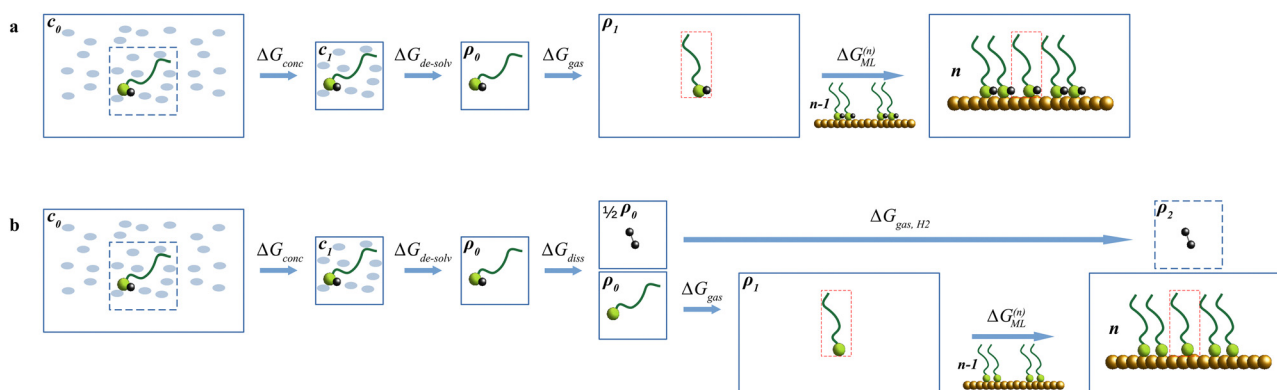
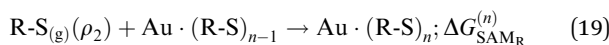
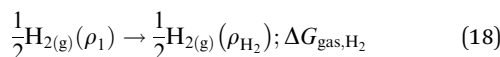
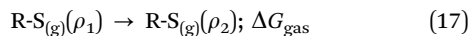
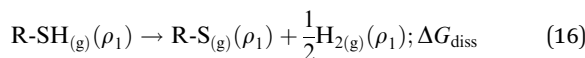
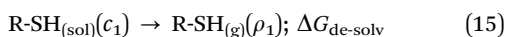
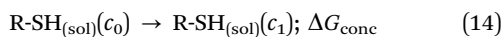


Fig. 3 Thermodynamic cycle for the double-decoupling calculations of the chemical potentials of the physisorbed (a) and chemisorbed (b) monolayers.



Reaction (2) can hence be split into the following steps:



and

$$\begin{aligned} \mu_S(n) = & \Delta G_{\text{conc}} + \Delta G_{\text{de-solv}} + \Delta G_{\text{diss}} + \Delta G_{\text{gas}} \\ & + \Delta G_{\text{gas,H}_2} + \Delta G_{\text{SAM}_R}^{(n)} \end{aligned} \quad (20)$$

The graphical summary for the chemisorption steps is given in Fig. 3(b).

## 3 Models and computational and experimental details

### 3.1 Model systems

The SAM models were composed of three-atom-thick Au(111) slabs covered by a variable number of physisorbed thiol molecules or chemisorbed thiyl radicals.

The gold slab model was obtained by optimizing a periodic three-layer-thick surface using CRYSTAL17 at the DFT/PW91 level; the cc-PVDz basis set was chosen, and Hay and Wadt's pseudopotentials were used for S and Au core electrons. The periodic slab for MD, containing 2187 gold atoms ( $27 \times 27 \times 3$ ), was cut out of the optimized surface and kept frozen during all the simulations.

We investigated SAMs formed either by 7-mercapto-4-methylcoumarin (MMC) and 3-mercapto-propanoic acid (MPA) or by the corresponding radical thiyls, indicated as MMCr and MPAr.

Structures, atomic partial charges and slightly modified GROMOS 54A7 force field parameters for the two thiols were obtained from the ATB website.<sup>43,44</sup> Atomic partial charges for thiyls were generated using the QEq equilibration method (with a  $10^{-6} e$  convergence). Initial geometries for molecular dynamics simulations were obtained by packing either molecules or radicals on the gold slab using the PACKMOL code:<sup>45</sup> a number of different initial densities were defined for the various species, as summarized in Table 1.

The calculation of  $\Delta G_{\text{de-solv}}$  was performed with MD simulations of a single thiol molecule with 2342 ethanol molecules in a cubic box of  $198.3 \text{ nm}^3$  volume, ensuring the proper solvent density at 298 K, using the GROMOS 54A7 force field.

Table 1 Initial density ranges for SAM MD simulations

SAM units	Adsorption process	Density range (molecules per $\text{nm}^2$ )
MMC	Physisorbed	0.56–5.03
	Chemisorbed	0.5–4.84
MPA	Physisorbed	0.56–7.45
	Chemisorbed	0.5–7.24

### 3.2 Gold–molecule interactions

While interactions between molecules in the monolayer can be expected to be accurately reproduced by GROMOS 54A7 force field parameters, the same cannot be granted for surface–molecule interactions. Hence, force field parameters for thiol/thiyl–gold interactions were optimized against DFT calculations on small model systems following the procedure described in ref. 46 (see in particular the ESI† of that publication for more details).

### 3.3 MD simulations

All the MD calculations were performed using the GROMACS software suite. The model systems were first minimized and then equilibrated for 200 ps at 300 K. The molecules to be decoupled from the environment to compute free energies (see below) were selected randomly from this pre-equilibrated system. Further minimization and equilibration for 200 ps at 300 K with a time step of 0.5 fs were then performed for each value of the decoupling parameter  $\lambda$ . Finally, for each  $\lambda$ , data were collected from a 1 ns simulation at 300 K with a timestep of 1 fs.

Both MMC and MPA in their undissociated (thiol) form showed dynamic instability at high SAM densities, leading some molecules to leave the monolayer, forming a sort of the “second layer” above the SAM. This would prevent the calculation of  $\Delta G_{\text{SAM}}^{(n)}$  with the method described below for some of the highest densities, so a mono-dimensional restraint was added in all the MD for thiols to limit the vertical motion with respect to the slab.

### 3.4 De-solvation and insertion free energies

The insertion ( $\Delta G_{\text{SAM}}^{(n)}, \Delta G_{\text{SAM}_R}^{(n)}$ ) and de-solvation ( $\Delta G_{\text{de-solv}}$ ) free energies were computed numerically from MD simulations, following the Bennet acceptance ratio (BAR) method.<sup>47</sup> Free energy differences are calculated by “switching off” the interactions between a single thiol molecule or thiyl radical and its environment, being a SAM on gold or a liquid solution (decoupling). As the accuracy of such free energy estimates depends on the overlap of the initial and final states,<sup>48</sup> the decoupling is commonly obtained as the succession of small steps where the interactions are slowly reduced.

In our setup, Coulomb interactions were switched off first, followed by Lennard–Jones interactions (using soft LJ potential energy functions to prevent divergence); in both cases, 20 steps were performed starting from the fully-interacting to the fully-decoupled system: considering the initial state, then a total of 41 MD simulations were required for each  $\Delta G$  calculation.

This procedure was performed once for each molecule in solution, while for SAMs it was replicated for each monolayer



density. Furthermore, to take into account the effects of SAM inhomogeneity, in each monolayer the calculation was repeated for 5 randomly chosen molecules/radicals, and the insertion  $\Delta G$  was computed as the mean of the 5 values.

### 3.5 Concentration free energy terms

As explained above, the calculation of SAM formation free energies includes two terms due to translational volume changes ( $\Delta G_{\text{conc}}$ ,  $\Delta G_{\text{gas}}$ ): they depend on the concentrations of thiol in ethanol ( $c_0$ ,  $c_1$ ) and on the gaseous densities ( $\rho_1$ ,  $\rho_2$ ).

We use  $c_0 = 0.1 \text{ mmol L}^{-1}$  as a typical concentration found in SAM synthesis, allowing a direct comparison with the experiments; the values of  $c_1$ ,  $\rho_1$  and  $\rho_2$  are derived from the MD simulation box volume. In the de-solvation process, a box of  $198.3 \text{ nm}^3$  is used, containing one thiol molecule (along with a suitable number of ethanol molecules in the condensed phase), so that  $c_1 = \rho_1 = 8.4 \text{ mmol L}^{-1}$ .

In steps (11) and (19), the simulation box volume is  $386.8 \text{ nm}^3$ , and a single molecule is decoupled from the monolayer, leading to  $\rho_2 = 4.3 \text{ mmol L}^{-1}$ . Then at  $T = 298 \text{ K}$  we have

$$\Delta G_{\text{conc}} = RT \ln(c_1/c_0) = 11.0 \text{ kJ mol}^{-1} \quad (21)$$

$$\Delta G_{\text{gas}} = RT \ln(\rho_2/\rho_1) = -1.7 \text{ kJ mol}^{-1} \quad (22)$$

### 3.6 Dissociation free energy

We computed the bond dissociation energies in the gas phase, treating all the species as ideal gases at thermodynamic equilibrium. The dissociation free energy,  $\Delta G_{\text{diss}}$ , can be obtained with the Gaussian program: the dissociation energy is computed at the DFT level, setting the suitable functional and basis sets; enthalpies and free energies are then obtained by adding vibrational, rotational and translational contributions for reagents and products. For (harmonic) vibrational terms, the second derivatives of the DFT energies are also computed at the same level as the energies. By default, the statistical thermodynamics is performed at  $298 \text{ K}$  and  $1 \text{ atm}$  ( $1.01325 \text{ bar}$ ), corresponding to a gas density of  $\rho_3 = 4.08 \times 10^{-2} \text{ mol L}^{-1}$ .

While experimental dissociation free energies are not available for the molecules of interest, their dissociation enthalpies are known better: so, as detailed in the ESI,<sup>†</sup> we used some experimental  $\Delta H_{\text{diss}}$  to set the best combination of density functional and basis set, and then compute at the same level  $\Delta G_{\text{diss}}$  for MMC and MPA.

Since  $\rho_3 \neq \rho_1$ , the latter being the density at which the de-solvation term is computed (see eqn (15) and Fig. 3), a further volume correction term should be added. However, the contributions from R-SH ( $\rho_1 \rightarrow \rho_3$ ) and from R-S ( $\rho_3 \rightarrow \rho_1$ ) before and after the dissociation, respectively, cancel out; on the other hand, the molecular hydrogen produced in the reaction does provide a density term,  $\Delta G_{\text{gas,H}_2}$ , discussed below.

### 3.7 H<sub>2</sub> concentration term

Under the experimental conditions, the radical formation does not occur in a closed system, and molecular hydrogen can evolve and leave the reaction. We assume that during the SAM

formation a small concentration of H<sub>2</sub> remains constant in the reaction environment, considering that the process occurs close to the gold surface, in the presence of denser and denser molecular layers and in contact with the solvent, all conditions that could hamper the gas evolution (but also making less and less reliable the ideal gas approximation!). In this model,  $\rho_{\text{H}_2}$  can be assigned a (presumably very low) constant value until the SAM growth stops at the maximum density. Assuming the ideal gas behaviour for H<sub>2</sub> and using  $P_{\text{H}_2}$  for the “steady state” hydrogen partial pressure (in bar), the correction term to be added to  $\Delta G_{\text{diss}}$  is

$$\Delta G_{\text{gas,H}_2} = \frac{1}{2} RT \ln(P_{\text{H}_2}/1.01325), \quad (23)$$

where the initial pressure ( $1 \text{ atm}$ ) corresponds to the standard conditions used by the Gaussian program to compute  $\Delta G_{\text{diss}}$ .

As we are not aware of any experimental determination of the hydrogen concentration at the monolayer level, we are left with the issue of estimating  $P_{\text{H}_2}$ .

The extreme case is  $\rho_{\text{H}_2} \rightarrow 0$ ,  $P_{\text{H}_2} \rightarrow 0$ , *i.e.* all the produced hydrogen leaves the reaction surroundings immediately, and this formally prevents the definition of a free energy change for the bond dissociation.

Avoiding this divergence, we restrict the model to two well-defined limiting cases, assuming that realistic scenarios should fall within these limits: in the first one,  $\Delta G_{\text{H}_2,\text{gas}} = 0$ , *i.e.* the hydrogen is produced in the standard state, with  $1 \text{ bar}$  partial pressure. In the second limit,  $\Delta G_{\text{H}_2,\text{gas}} = -\Delta G_{\text{diss}}$ , *i.e.* the concentration term balances the dissociation free energy completely, which corresponds to extremely low concentrations/partial pressures (anticipating the results illustrated in the next section, the H<sub>2</sub> pressure should be around  $10^{-23} \text{ bar}$ , *i.e.* about 13 orders of magnitude lower than the partial pressure of hydrogen in the atmosphere).

Both these limits appear unrealistic: most likely, in real experiments H<sub>2</sub> will be produced at some intermediate concentration, with effects on the SAM chemical potential discussed below.

### 3.8 Helmholtz and Gibbs free energies

To improve the simulation stability, we adopted *NVT* ensembles in the calculation with the BAR method of free energy changes for reactions (11) and (19). This provides Helmholtz ( $\Delta A$ ), rather than Gibbs ( $\Delta G$ ) free energies: the latter can be obtained by evaluating the factor  $PV$  for products and reactants. The correction can be likely neglected for the monolayers (which are condensed phases) but it has to be included for the (ideal) gaseous thiol/thiyl molecule, leading to

$$\Delta G_{\text{SAM}} = \Delta A_{\text{SAM}} - RT = \Delta A_{\text{SAM}} - 2.5 \text{ kJ mol}^{-1} \quad (24)$$

at  $T = 298 \text{ K}$ ; the same applies to  $\Delta G_{\text{SAM,R}}$ .

### 3.9 Experimental MMC and MPA surface densities

As previously presented,<sup>42</sup> the quantitative determination of the surface density of SAMs can be conducted through reference-free grazing-incidence X-ray fluorescence (RF-GIXRF).<sup>49</sup> This method allows the mass per area of a given target element to be derived from the detected X-ray fluorescence signal



employing physically calibrated instrumentation<sup>50</sup> and tabulated<sup>51</sup> or experimentally determined atomic fundamental parameters.<sup>52</sup> To determine the density of MMC and MPA, we used sulfur as the target atom to find its mass density  $\sigma_s$  through eqn (25).<sup>53</sup>

$$\sigma_s = \frac{1}{k} \cdot N \cdot \frac{P_{S,K}}{\varepsilon(E_{S,K}) \cdot I_{XSW}(E_0, \theta) \cdot \tau_{S,K}(E_0) \cdot \omega_{S,K}} \quad (25)$$

where the factor  $N$  depends on the experimental setup parameters, *i.e.* solid angle of detection, angle of incidence and incoming photon flux. The photon count rate  $P_{S,K}$  is normalized to instrumental and atomic fundamental parameters already discussed in ref. 42, 46 and 53. For the RF-GIXRF experiment, we used SAMs formed on a virtually flat gold layer on silicon. The roughness of the gold layer induces a change in the surface area, and the ratio between the surface area and the flat projected area is  $k$  in eqn (25). Atomic force microscopy (AFM) scans on the gold surface determined the correction factor  $1/k = (0.9925 \pm 0.0014)$  in eqn (25). Each gold-covered substrate was cleaned with O<sub>2</sub> plasma and then incubated for two hours in an ethanol-based solution with 0.1 mM MMC or MPA. Subsequently, the substrates were abundantly washed with ethanol to eliminate any unbound molecules. The fluorescence spectra were acquired in different points of the SAM and on a non-functionalized gold substrate to account for any sulfur-based contamination. The mass density of sulfur is converted to the molecular surface density by multiplying it to  $N_A/w_s$ , respectively, the Avogadro number and sulfur atom weight, considering that each molecule contains only a S atom localized in the anchor group. For each of the tested molecules, the values of  $\sigma_s$  carry a relative uncertainty of 11% due to the single terms in eqn (25) where the largest uncertainty contribution is given by the fluorescence yield  $\omega_{S,K}$  reported at the denominator.<sup>53</sup>

## 4 Results and discussion

### 4.1 Experimental MMC and MPA surface densities

The RF-GIXRF quantification yielded a surface density value of  $(4.1 \pm 0.6)$  MMC molecules per nm<sup>2</sup> and  $(7.6 \pm 1.1)$  MPA molecules per nm<sup>2</sup>. The uncertainties are due to the propagation of uncertainties for independent measurements. The density measured for MPA is quite high compared to the regular geometrical model mentioned in the Introduction section: this value, however, is comparable within the uncertainty to the densities found with inductively coupled plasma mass spectrometry<sup>40,41</sup> (see above). A part of the recorded signal could be ascribed to thiol molecules adsorbed on top of the monolayer, held by van der Waals interactions and H-bonds despite the accurate ethanol rinsing applied to the samples. In a previous work,<sup>42</sup> we investigated the oxidation state of MMC SAM sulfur atoms through X-ray photoelectron spectroscopy (XPS), finding a minor component in the XPS spectra compatible with unbound undissociated thiols, along with a major contribution from chemisorbed thiyls: the former could be due to MMC molecules lying on top of the SAM, and a similar hypothesis is possible for MPA, whose acid group could form even stronger intermolecular interactions. In this case, the measured densities

have to be considered as upper bounds when compared with the simulations.

### 4.2 Common concentration terms

The chemical potentials for (physisorbed) thiol and (chemisorbed) thiyl SAMs at various surface densities were computed with eqn (12) and (20), respectively.

The concentration terms are common to all the simulated systems with the values  $\Delta G_{\text{conc}} = 11.0 \text{ kJ mol}^{-1}$  and  $\Delta G_{\text{gas}} = -1.7 \text{ kJ mol}^{-1}$ , as reported in the previous section; the other contributions have to be computed for MMC and MPA separately.

### 4.3 MMC

The MMC thiol de-solvation energy, from ethanol to the gas phase, was computed with the BAR method, obtaining  $\Delta G_{\text{de-solv}} = 17.9 \text{ kJ mol}^{-1}$ . The MMC dissociation energy was computed using the Gaussian program at the DFT level, with the B3P86 functional and cc-pVTZ basis set, as described in the ESI:† the best estimate is  $\Delta G_{\text{diss}} = 130 \text{ kJ mol}^{-1}$ .

The remaining contributions,  $\Delta G_{\text{SAM}}^{(n)}$  or  $\Delta G_{\text{SAM}_R}^{(n)}$ , due to MMC insertion into an existing SAM of density  $n$  were evaluated with the BAR method as the negative of the free energy of removal of one molecule/radical from the SAM. To account for possible layer inhomogeneities, 5 molecules or radicals were chosen randomly in each SAM and decoupled from the system, averaging the corresponding removal free energies. All the results are reported in the ESI.†

The resulting chemical potentials are illustrated in Fig. 4. As noted in the previous section, the potential for chemisorbed thiyls contains a term that depends on the (unknown) concentration of H<sub>2</sub> produced in the dissociation reaction: two limiting cases are shown in Fig. 4, namely H<sub>2</sub> at standard pressure (leading to  $\Delta G_{\text{H}_2, \text{gas}} = 0$ ) or at extremely low pressure, so that  $\Delta G_{\text{diss}} + \Delta G_{\text{H}_2, \text{gas}} = 0$ : likely, the real value falls between these extremes.

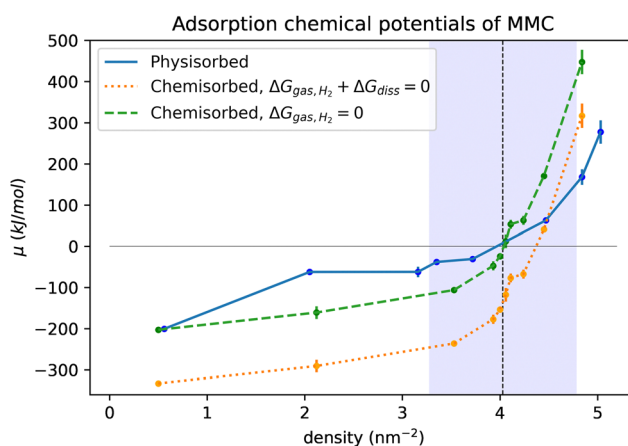


Fig. 4 Calculated chemical potential of physisorbed and chemisorbed MMC SAMs at different densities. The vertical dotted line indicates the experimental value (see text) and the shaded area shows the corresponding experimental uncertainty; the two curves for chemisorbed thiyls correspond to different assumptions about the equilibrium concentration of gaseous H<sub>2</sub>.



For both chemisorbed and physisorbed SAMs, the chemical potential grows slowly at low densities, corresponding to the striped (lying down) phase, until about 3.5 molecules per  $\text{nm}^2$ . Above this density, the (physisorbed) thiol SAM chemical potential rises steeply as the “standing up” phase appears and spreads. The same happens for the chemisorbed thiy l SAMs, whose chemical potential rises even more sharply: the two curves corresponding to the limiting cases mentioned above are parallel, with a distance equal to the dissociation free energy. Crossing of the  $\mu = 0$  line, indicating thermodynamic instability for very dense layers, occurs at about 4 molecules per  $\text{nm}^2$  for physisorbed SAMs; chemisorbed monolayers become unstable between 4 and 4.5 molecules per  $\text{nm}^2$  depending on the pressure of  $\text{H}_2$  in the dissociation reaction. All these values are compatible with the measured MMC SAM density reported above: the calculated chemical potentials, however, appear to favor the chemisorbed thiy l SAMs in the whole range of the monolayer thermodynamic stability.

#### 4.4 MPA

The same approach as above was applied to MPA SAMs: the desolvation free energy,  $\Delta G_{\text{de-solv}} = 55.8 \text{ kJ mol}^{-1}$ , is much larger than that for MMC, since the thiol is polar and able to form hydrogen bonds with the solvent. The dissociation free energy was computed at the DFT level with B3P86/cc-pVTZ again, obtaining  $\Delta G_{\text{diss}} = 120 \text{ kJ mol}^{-1}$ . Insertion free energies were computed as above by averaging the results for 5 molecules or radicals from each SAM.

The chemical potentials of physisorbed and chemisorbed MPA monolayers are reported for various densities in Fig. 5: as in MMC, the potentials show a plateau for densities below 3 molecules per  $\text{nm}^2$ , though in this case with a very small negative slope, probably because the striped phase is more and more stabilized by hydrogen bonds between neighboring molecules or radicals.

At higher densities, the chemical potential rises, as the standing up phase appears and spreads: for physisorbed molecules, the free energy becomes positive around 3.8 molecules per  $\text{nm}^2$ , while chemisorbed radical monolayers become unstable between 3.8 and 5.8 molecules per  $\text{nm}^2$ . Chemical potentials rise less steeply for MPA than for MMC, so the crossing of the  $\mu = 0$  line occurs over a larger density range: unlike the MMC case, for MPA only the (chemisorbed) thiy l SAMs are compatible with the experimental density (provided that the equilibrium  $\text{H}_2$  concentration is very small, so the real curve approaches the limit of  $\Delta G_{\text{diss}} + \Delta G_{\text{H}_2, \text{gas}} = 0$ ).

This is a significant result, indeed, since the debate on the chemical nature of the monolayers is still intense as noted in the Introduction section: at least for MPA, the present chemical potential calculations clearly show that the density can reach values close to the experimental measures only in the case of radical thiy l SAMs.

Then, the chemisorbed SAMs formed by radical thiy ls are found to be thermodynamically favored with respect to the undissociated physisorbed phase: for MMC this result does not

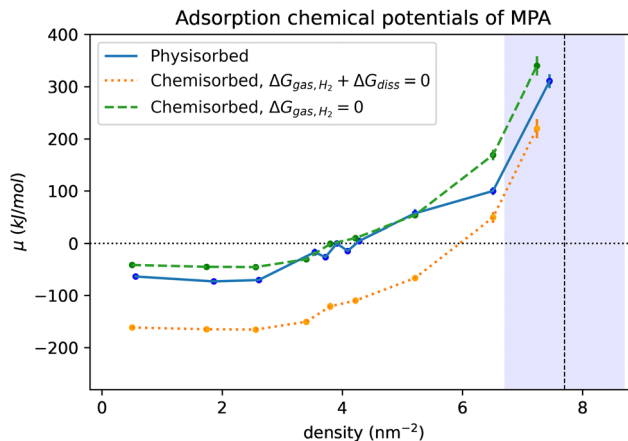


Fig. 5 Calculated chemical potential of physisorbed and chemisorbed MPA SAMs at different densities. The vertical dotted line indicates the experimental value (see text) and the shaded area shows the corresponding experimental uncertainty; the two curves for chemisorbed thiy ls correspond to different assumptions about the equilibrium concentration of gaseous  $\text{H}_2$ .

change, qualitatively, even considering very different values for the S–H dissociation energy; for MPA it holds assuming a low concentration for the evolved gaseous hydrogen, but it is reinforced by the comparison with the experimental density. We noted above that the experimental uncertainty can be larger than the instrumental contribution shown in Fig. 4 and 5 for the possible presence of some molecules lying on top of the SAMs. Anyway, even considering the smaller density reported in the literature for MPA monolayers, around 4.6 molecules per  $\text{nm}^2$  as recalled in the Introduction section, the comparison with the theoretical values in Fig. 5 suggests that MPA monolayers are formed by radical thiy ls, with a steady concentration of gaseous hydrogen intermediate between the two considered extreme cases.

Since in our approach the SAM formation process is split into successive steps, computing the free energy changes separately, one can see that the prevalence of the chemisorbed phase is due to the interaction with the gold atoms, much larger for radical sulfur than for the thiol group, despite the large dissociation energy required. Desolvation free energies and molecule–molecule side interactions, on the other hand, do not affect the balance between physisorbed and chemisorbed phases significantly.

A further comment can be useful about the transferability of the present model. The main source of uncertainty in the computed chemical potentials comes from the dissociation process, whose  $\Delta G$  depends dramatically on the assumed equilibrium concentration of  $\text{H}_2$ : this is expected to hold for any other thiol/thiy l couple under the same conditions, so the physisorbed/chemisorbed balance will always be determined with such a large uncertainty. On the other hand, we have shown that all the other thermodynamic contributions can be effectively computed with our method, and this led us to conclude that both MMC and MPA SAM are likely to be formed by radical thiy ls rather than undissociated thiols. Other systems will differ for the entity of sulfur/gold and especially intermolecular interactions,



and we believe that the approach described here is well suited to compute the chemical potentials for these terms with the same accuracy as in the present case.

## 5 Conclusions and outlook

We described a computational procedure to evaluate the chemical potential of thiol/thiyl SAMs based on the analysis of molecular dynamics data. Compared to the models based on electronic structure calculations, the present approach includes a much larger description of thermal contributions to enthalpies and entropies, and it allows the simulation of large monolayers, so formation free energies can be computed as a function of SAM densities, with accuracy mostly dependent on the force field quality.

This procedure was applied to 7-mercapto-4-methylcoumarin (MMC) and 3-mercapto-propanoic acid (MPA) on a flat (111) Au surface at various monolayer densities; both thiol and thiyl SAMs were considered to investigate whether the maximum attainable densities differ for molecules (R-SH) and radicals (R-S), thus contributing to the debate on the chemical nature of these systems.

The chemical potential is defined as the free energy change when a thiol molecule leaves a 0.1 mmol L<sup>-1</sup> ethanol solution and enters a pre-formed monolayer on a flat Au surface, possibly dissociating the S-H bond in the case of radical thiyl SAMs. Since this quantity depends on the layer density, one can find how many molecules or radicals can be added to the SAM before the chemical potential becomes positive, and the layer growth is thermodynamically unfavored.

The results can be compared with the experimental measure of MMC and MPA monolayer densities, performed with the RF-GIXRF method. For MMC, the maximum theoretical densities of both thiol and thiyl SAMs agree with the experimental data; for MPA, on the other hand, only the radical thiyl model is compatible with the experimental density, though the calculation provides a slightly lower density.

Our calculations of thermodynamic stability, then, suggest that the monolayers are formed by thiyl radicals, rather than undissociated thiols, contributing to clarifying the debated chemical nature of these SAMs.

## Author contributions

A. Z., M. C. and D. M. performed theoretical calculations; P. K. performed AFM measurements; E. C. and F. F. L. performed sample preparation; P. H. and Y. K. performed GIXRF measurements; P. H. and E. C. performed data analysis; F. F. L., B. B. and M. C. provided funding; A. Z., M. C. and E. C. wrote the paper.

## Data availability

The data supporting this article have been included as part of the ESI.†

## Conflicts of interest

There are no conflicts to declare.

## Acknowledgements

A. Z., D. M. and M. C. acknowledge the financial support by Università del Piemonte Orientale (through the FAR funding program). E. C., F. F. L., P. H. and B. B. acknowledge the project 21GRD01 OpMetBat. The project has received funding from the European Partnership on Metrology, cofinanced by the European Union's Horizon Europe Research and Innovation Programme and by Participating States.

## References

- 1 J. L. Wilbur and G. M. Whitesides, *Nanotechnology*, Springer, 1999, pp. 331–369.
- 2 B. D. Gates, Q. Xu, M. Stewart, D. Ryan, C. G. Willson and G. M. Whitesides, *Chem. Rev.*, 2005, **105**, 1171–1196.
- 3 J. C. Love, L. A. Estroff, J. K. Kriebel, R. G. Nuzzo and G. M. Whitesides, *Chem. Rev.*, 2005, **105**, 1103–1170.
- 4 J. A. Rogers and R. G. Nuzzo, *Mater. Today*, 2005, **8**, 50–56.
- 5 B. Ziaie, A. Baldi and M. Z. Atashbar, *Springer Handb. Nanotechnol.*, 2010, 231–269.
- 6 A. Terfort and M. Zharnikov, *Adv. Mater. Interfaces*, 2021, **8**, 2100148.
- 7 J. M. Tour, *Acc. Chem. Res.*, 2000, **33**, 791–804.
- 8 D. Xiang, X. Wang, C. Jia, T. Lee and X. Guo, *Chem. Rev.*, 2016, **116**, 4318–4440.
- 9 B. Chen and K. Xu, *NANO*, 2019, **14**, 1–19.
- 10 G. Kong, S. Byeon, S. Park, H. Song, S.-Y. Kim and H. Yoon, *Adv. Electron. Mater.*, 2020, **6**, 1901157.
- 11 Y. Liu, X. Qiu, S. Soni and R. C. Chiechi, *Chem. Phys. Rev.*, 2021, **2**, 021303.
- 12 R. Gupta, J. A. Fereiro, A. Bayat, A. Pritam, M. Zharnikov and P. C. Mondal, *Nat. Rev. Chem.*, 2023, **7**, 106–122.
- 13 B. Bonanni, A. R. Bizzarri and S. Cannistraro, *J. Phys. Chem. B*, 2006, **110**, 14574–14580.
- 14 E. T. Castellana and P. S. Cremer, *Surf. Sci. Rep.*, 2006, **61**, 429–444.
- 15 D. Samanta and A. Sarkar, *Chem. Soc. Rev.*, 2011, **40**, 2567–2592.
- 16 T. Zeng, R. P. Gautam, D. H. Ko, H.-L. Wu, A. Hosseini, Y. Li, C. J. Barile and E. C. Tse, *Nat. Rev. Chem.*, 2022, **6**, 862–880.
- 17 C. Vericat, M. Vela, G. Benitez, P. Carro and R. Salvarezza, *Chem. Soc. Rev.*, 2010, **39**, 1805–1834.
- 18 E. Pensa, E. Cortés, G. Corthey, P. Carro, C. Vericat, M. H. Fonticelli, G. Benitez, A. A. Rubert and R. C. Salvarezza, *Acc. Chem. Res.*, 2012, **45**, 1183–1192.
- 19 M. Inkpen, Z.-F. Liu, H. Li, L. Campos, J. Neaton and L. Venkataraman, *Nat. Chem.*, 2019, **11**, 351–358.
- 20 I. I. Rzeźnicka, J. Lee, P. Maksymovych and J. T. Yates, *J. Phys. Chem. B*, 2005, **109**, 15992–15996.
- 21 L. Kankate, A. Turchanin and A. Götzhäuser, *Langmuir*, 2009, **25**, 10435–10438.



- 22 N. B. Luque, E. Santos, J. Andres and F. Tielens, *Langmuir*, 2011, **27**, 14514–14521.
- 23 F. Tielens and E. Santos, *J. Phys. Chem. C*, 2010, **114**, 9444–9452.
- 24 G. Rajaraman, A. Caneschi, D. Gatteschi and F. Totti, *Phys. Chem. Chem. Phys.*, 2011, **13**, 3886–3895.
- 25 H. Guesmi, N. B. Luque, E. Santos and F. Tielens, *Chem. – Eur. J.*, 2017, **23**, 1402–1408.
- 26 J. K. Roy, E. S. Vasquez, H. P. Pinto, S. Kumari, K. B. Walters and J. Leszczynski, *Phys. Chem. Chem. Phys.*, 2019, **21**, 23320–23328.
- 27 J. R. Reimers, D. Panduwina, J. Visser, Y. Chin, C. Tang, L. Goerigk, M. J. Ford, M. Santic, T. J. Sum, M. J. Coenen, B. L. Hendriksen, J. A. Elemans, N. S. Hush and M. J. Crossley, *Proc. Natl. Acad. Sci. U. S. A.*, 2015, **112**, E6101–E6110.
- 28 E. Pensa, L. M. Azofra, T. Albrecht, R. C. Salvarezza and P. Carro, *J. Phys. Chem. C*, 2020, **124**, 26748–26758.
- 29 M. K. Gilson, J. A. Given, B. L. Bush and J. A. McCammon, *Biophys. J.*, 1997, **72**, 1047–1069.
- 30 J. Wang, Y. Deng and B. Roux, *Biophys. J.*, 2006, **91**, 2798–2814.
- 31 Y. Deng and B. Roux, *J. Chem. Theory Comput.*, 2006, **2**, 1255–1273.
- 32 Y. Deng and B. Roux, *J. Phys. Chem. B*, 2009, **113**, 2234–2246.
- 33 R. Salari, T. Joseph, R. Lohia, J. Hénin and G. Brannigan, *J. Chem. Theory Comput.*, 2018, **14**, 6560–6573.
- 34 E. Duboué-Dijon and J. Hénin, *J. Chem. Phys.*, 2021, **154**, 204101.
- 35 L. Li, T. Totton and D. Frenkel, *J. Chem. Phys.*, 2017, **146**, 214110.
- 36 G. Gobbo, G. Ciccotti and B. L. Trout, *J. Chem. Phys.*, 2019, **150**, 201104.
- 37 D. L. Mobley and G. Duarte Ramos Matos, *F1000Research*, 2018, **7**, 1–22.
- 38 X. Zhang, R. S. Defever, S. Sarupria and R. B. Getman, *J. Chem. Inf. Model.*, 2019, **59**, 2190–2198.
- 39 F. Schreiber, *Prog. Surf. Sci.*, 2000, **65**, 151–257.
- 40 H. Hinterwirth, S. Kappel, T. Waitz, T. Prohaska, W. Lindner and M. Lämmerhofer, *ACS Nano*, 2013, **7**, 1129–1136.
- 41 S. Elzey, D.-H. Tsai, S. A. Rabb, L. L. Yu, M. R. Winchester and V. A. Hackley, *Anal. Bioanal. Chem.*, 2012, **403**, 145–149.
- 42 D. Marchi, E. Cara, F. F. Lupi, P. Hönicke, Y. Kayser, B. Beckhof, M. Castellino, P. Klapetek, A. Zoccante, M. Laus and M. Cossi, *Phys. Chem. Chem. Phys.*, 2022, **24**, 22083–22090.
- 43 A. K. Malde, L. Zuo, M. Breeze, M. Stroet, D. Poger, P. C. Nair, C. Oostenbrink and A. E. Mark, *J. Chem. Theory Comput.*, 2011, **7**, 4026–4037.
- 44 M. Stroet, B. Caron, K. M. Visscher, D. P. Geerke, A. K. Malde and A. E. Mark, *J. Chem. Theory Comput.*, 2018, **14**, 5834–5845.
- 45 L. Martínez, R. Andrade, E. G. Birgin and J. M. Martínez, *J. Comput. Chem.*, 2009, **30**, 2157–2164.
- 46 E. Cara, L. Mandrile, A. Sacco, A. M. Giovannozzi, A. M. Rossi, F. Celegato, N. De Leo, P. Hönicke, Y. Kayser, B. Beckhoff, D. Marchi, A. Zoccante, M. Cossi, M. Laus, L. Boarino and F. Ferrarese Lupi, *J. Mater. Chem. C*, 2020, **8**, 16513–16519.
- 47 C. H. Bennett, *J. Comput. Phys.*, 1976, **22**, 245–268.
- 48 A. Pohorille, C. Jarzynski and C. Chipot, *J. Phys. Chem. B*, 2010, **114**, 10235–10253.
- 49 P. Hönicke, B. Detlefs, E. Nolot, Y. Kayser, U. Mühle, B. Pollakowski and B. Beckhoff, *J. Vac. Sci. Technol., A*, 2019, **37**, 041502.
- 50 J. Lubeck, B. Beckhoff, R. Fliegau, I. Holfelder, P. Hönicke, M. Müller, B. Pollakowski, F. Reinhardt and J. Weser, *Rev. Sci. Instrum.*, 2013, **84**, 045106.
- 51 T. Schoonjans, A. Brunetti, B. Golosio, M. S. Del Rio, V. A. Solé, C. Ferrero and L. Vincze, *Spectrochim. Acta, Part B*, 2011, **66**, 776–784.
- 52 P. Hönicke, R. Unterumsberger, N. Wauschkuhn, M. Krämer, B. Beckhoff, P. Indelicato, J. Sampaio, J. P. Marques, M. Guerra, F. Parente and J. P. Santos, *Radiat. Phys. Chem.*, 2023, **202**, 110501.
- 53 B. Beckhoff, *J. Anal. At. Spectrom.*, 2008, **23**, 845–853.

